Unified Control of an Orbital Manipulator for the Approach and Grasping of a Free-floating Satellite

Ria Vijayan[1], Marco De Stefano[1], Alexander Dietrich[1] and Christian Ott[2]

***Abstract*—In robotic on-orbit servicing missions, an orbital manipulator approaches and grasps a faulty client satellite. The approach phase and post-grasp phase pose different challenges and hence impose different requirements on the design of a controller for the orbital manipulator. In the approach phase, the foremost requirement is to track the client satellite with the end-effector in Cartesian space. Additionally, it is desirable to have the servicing satellite and arm in a suitable safe configuration during grasp and stabilization. In the post-grasp phase, a crucial requirement is to limit the interaction forces at the manipulator's end-effector. This is to ensure that the grasping interface is not damaged during stabilization. In this paper, we develop a unified control framework for an orbital manipulator in the approach phase and post-grasp phase. The controller hierarchically fulfills various requirements of each phase. In the approach phase, the proposed controller tracks the Cartesian pose of the grasp point on the client. It also simultaneously tracks a joint-space trajectory in the nullspace to achieve a suitable servicer pose for grasping. The proposed post-grasp controller stabilizes the client with limited interaction forces while bringing the servicer to a safe configuration with respect to the client. Furthermore, the unified controller redistributes torques between thrusters and reaction wheels so as to save thruster energy in the approach phase and reduce external momentum in the post-grasp phase. Results of simulation and experiments performed on the hardware-in-the-loop facility OOS-Sim at DLR validate the proposed method.**

***Index Terms*—On orbit servicing, post-grasp, orbital robotic manipulator, reaction wheels, hierarchical control.**

I. Introduction

THE use of a robotic manipulator offers a promising alternative to the cost, risk, and limited reach of sending humans into space for on-orbit servicing (OOS) missions. In the context of OOS, we consider a spacecraft equipped with a manipulator arm, the *servicer*, which approaches and grasps a *client* satellite to perform servicing tasks such as maintenance or repair in orbit. The client is a free-floating uncooperative satellite in the sense that it features no functioning guidance, navigation, and control capabilities. We define the *approach* phase when the motion towards capture/grasp is initiated with the client in the close vicinity of the servicing manipulator's workspace (as in Fig. 1). Following the capture we enter the *post-grasp* stabilization phase. By stabilization, we refer to the damping of the client's momentum post-capture.

Robotic solutions for OOS tasks were demonstrated in recent mission studies, see e.g. the e.Deorbit or DEOS mission [1], [2], the COMRADE project [3] or the survey on robotics in space in [4]. Since defunct satellites usually still have a residual spin velocity, e.g. 1 deg/s as reported in [5], the capture of such a spinning client will inevitably transfer momentum to the servicer. Thus, a post-grasp stabilization strategy is required before performing servicing tasks [3].

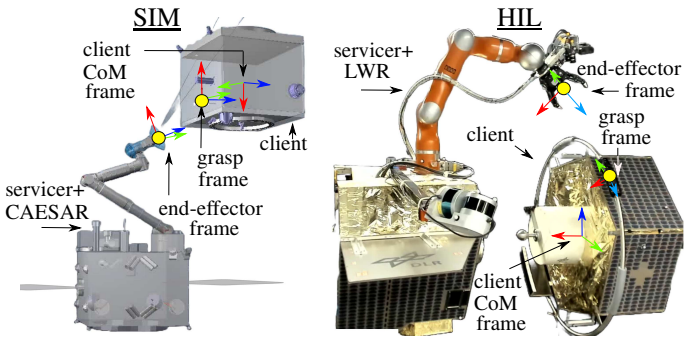

Fig. 1: Simulation (SIM) and hardware-in-the-loop (HIL) setup with relevant frames (RGB≡XYZ) used for the analysis/experiments. Both setups show a servicer satellite equipped with a manipulator (CAESAR/LWR) and a client satellite with a grasping interface.

The advantages of using coordinated control (control of manipulator and base motion) of a space robot for the approach phase have already been demonstrated e.g. in [6]–[8] (for further reading see surveys [4], [9], [10]). In [11], the reaction null space is used to transfer the impact momentum from the base to the manipulator. In [12], a virtual-mass for impedance matching control was introduced to maintain contact with the client. Impact minimization during capture was analyzed in [13] using the center of percussion concept. In [14] a strategy to remove the accumulated momentum from contacts during the capture phase is presented. In [15], the approach of a servicer tangential to the grasping point trajectory is analyzed.

A challenge in the post-grasp phase is to limit the interaction forces at the grasping interface of the manipulator's end-effector. This is required to gently transfer momentum [4], [16] and avoid mechanical damage during stabilization [17]–[19]. Approaches [17], [19], [20] rely on force/torque measurements for direct force control. In [21] this was done without force feedback, considering 6 degrees-of-freedom (DoF) external actuation on the servicer, e.g. thrusters. In [22] we designed a controller for initializing berthing using reaction wheels, considering the post-stabilization phase with zero momentum. Therefore, a unified control strategy that complements thrusters with reaction wheels presents a pragmatic solution to minimize thrust utilization in the approach phase and partially dump and transfer momentum incurred during the grasp phase.

[1] The authors are with the Institute of Robotics and Mechatronics, German Aerospace Center (DLR), 82234 Wessling, Germany.

[2] The author is with TU Wien and German Aerospace Center (DLR).

A supplementary video of the experiments accompanies this manuscript.

Contact: Ria.Vijayan@dlr.de. Manuscript submitted on 07 August 2024.

 DOI: 10.1109/TMECH.2025.3545201

In this paper, we propose a unified coordinated control strategy for the approach-to-grasp and post-grasp phases using a hierarchical control based on nullspace projections. In [21], [22] we focused only on the post-grasp phase with a regulation controller. Here we unify the control from the approach phase to post-grasp phase, including contact phase, while designing a tracking controller. In [21] we designed a controller for the post-grasp phase using only thrusters to dump momentum while limiting forces. Here we exploit the redundant DoF provided by the reaction wheels of a servicer to save thruster energy during the approach phase and complement thruster limits in the post-grasp phase. This is done by adapting the optimization-based algorithm in [23] to perform the torque redistribution in nullspace coordinates instead of generalized coordinates. Beneficially, this reduces the dimension of the optimization to only the redundant DoF. The task of post-grasp stabilization of the servicer is designed to not influence the interaction forces by exploiting end-effector's nullspace. The contributions of this work are summarized as follows:

- A control framework which allows the inclusion of constraints through quadratic-programming (QP) based adaptations within the nullspace projection-based control paradigm.
- A unified controller using the above framework, for the approach phase and post-grasp phase, that respects multiple space mission constraints. In addition to limiting the interaction forces at the manipulator's end-effector, thruster limits are tackled through redistribution of reaction wheel torques within the nullspace.
- Experimental validation on a hardware-in-the-loop robotic facility (see accompanying video[1]).

The structure of the paper is as follows. Sec. II presents the motivation, objectives, and preliminaries on the dynamic modeling for the approach phase and post-grasp phase. Sec. III presents the design of the unified controller for the proposed strategies in the approach phase and post-grasp phase. Sec. IV presents the results of simulation and experiment performed on the HIL facility, OOS-Sim, at DLR [24] (see Fig. 1). Sec. V concludes the work.

II. Objectives & Preliminaries

The scenario of interest is the approach and capture of a client satellite, which spins along its major axis, using an orbital manipulator. In this situation, joint limits, singularity of the manipulator, and/or undesirable displacement of the base [25], [26], can result in compromising the approach-to-grasp and post-grasp stabilization, thus, leading to mission failure. This problem can be observed in a simulation and hardware analysis shown in Fig. 2. Using a free-floating (unactuated base) strategy with a spinning satellite could result in the arm losing its manipulability (Fig. 2 left, *approach phase*) and the base colliding with the client (Fig. 2 right, *post-grasp phase*).

Therefore, a free-flying (actuated base) control strategy for the *approach phase* with two Cartesian tasks – one at the end-effector for grasping and one at the base for configuration safety, may be employed. For a redundant arm using nullspace-based potentials, this strategy may not always lead to a desirable manipulator configuration. We propose instead to have one Cartesian task at the end-effector and a secondary task on the joint pose in the nullspace. This desirable joint pose can further be chosen such as to ensure better manipulability and workspace constraints like joint limits and self-collisions [27], [28].

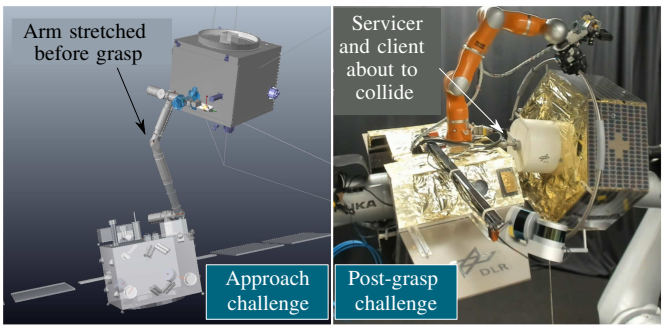

Fig. 2: Problem statement. Left: arm with low manipulability before approaching grasp. Right: servicer and client in an unsafe configuration during post-grasp stabilzation.

The challenge of configuration safety also applies to the *post-grasp phase*. To avoid the risk of collision highlighted in Fig. 2 right, simply applying a potential on the joints (or base) in parallel with the Cartesian potential at the end-effector, leads to higher interaction forces at the grasp interface of the captured client. High interaction forces must be avoided at the grasp interface [17], [19]. We propose to avoid this by applying the secondary potential in the nullspace of the end-effector, thus, beneficially isolating the interaction forces from the configuration task. Demanding a certain manipulator configuration in the nullspace has the implication of keeping the servicer's base at a safe distance from the client. Further, the interaction forces from the Cartesian stabilization task at the end-effector shall be limited explicitly by augmenting the controller with a QP-based algorithm.

In addition, accounting for thruster limits represents a key requirement for a space mission. This is proposed to be dealt with by using reaction wheels to complement thrusters, and designing a QP-based optimal torque distribution strategy for each of the phases.

Against this background, we define a set of tasks summarized in Table I as the proposed objectives to be fulfilled by the controller in the approach and post-grasp phases. The tasks defined in Table I will then allow a safe approach and capture of a spinning satellite while tackling the problems in Fig. 2.

Preliminaries

We consider a servicer consisting of a base spacecraft equipped with r reaction wheels and an n-DoF manipulator. The client is an unactuated floating satellite. At the start of the approach phase, we consider the servicer's initial velocity to be zero. The servicer and client dynamics are given by

$$\boldsymbol{M}_s(\boldsymbol{q})\dot{\boldsymbol{v}}_s + \boldsymbol{C}_s(\boldsymbol{q},\dot{\boldsymbol{q}})\boldsymbol{v}_s = \boldsymbol{\Gamma} + \boldsymbol{J}_e^T(\boldsymbol{q})\boldsymbol{F}_c \tag{1}$$

$$\boldsymbol{M}_c\dot{\boldsymbol{v}}_c + \boldsymbol{C}_c(\boldsymbol{v}_c)\boldsymbol{v}_c = -\boldsymbol{J}_c^T\boldsymbol{F}_c, \tag{2}$$

[1]A supplementary video of the experiments accompanies this manuscript..

TABLE I: Proposed control objectives for the approach phase and post-grasp phase in decreasing order of priority.

Task (subsystem)	**Approach-to-grasp phase**	**Post-grasp phase**
T1 (end-effector)	Track client grasping point with end-effector	Stabilize client while limiting interaction forces at end-effector
T2 (manipulator joints)	Follow joint trajectory for desirable pose at grasp	Damp out joint velocities and reach a safe configuration
T3 (reaction wheels)	Use reaction wheels to minimize thruster actuation	Dissipate gained external momentum with thruster actuation

where, $\boldsymbol{M}_s, \boldsymbol{C}_s \in \mathbb{R}^{(6+n)\times(6+n+r)}$ and $\boldsymbol{M}_c, \boldsymbol{C}_c \in \mathbb{R}^{6\times6}$, are the inertia and Coriolis/centrifugal matrices of the servicer and client, respectively. The client dynamic parameters here are assumed to be known. The servicer velocity is $\boldsymbol{v}_s = \begin{bmatrix}\boldsymbol{v}_b^T & \dot{\boldsymbol{q}}_n^T & \dot{\boldsymbol{q}}_r^T\end{bmatrix}^T \in \mathbb{R}^{6+n+r}$, with the Cartesian velocity (linear and angular) of the base $\boldsymbol{v}_b \in \mathbb{R}^6$, manipulator joint rates $\dot{\boldsymbol{q}}_n \in \mathbb{R}^n$, and reaction wheel rates $\dot{\boldsymbol{q}}_r \in \mathbb{R}^r$. The actuation on the servicer $\boldsymbol{\Gamma} = \begin{bmatrix}\boldsymbol{F}_b^T & \boldsymbol{\tau}_n^T & \boldsymbol{\tau}_r^T\end{bmatrix}^T \in \mathbb{R}^{6+n+r}$ includes the base thruster force and torque ($\boldsymbol{F}_b = \begin{bmatrix}\boldsymbol{f}_b^T & \boldsymbol{\tau}_b^T\end{bmatrix}^T \in \mathbb{R}^6$), manipulator torques ($\boldsymbol{\tau}_n \in \mathbb{R}^n$), and reaction wheels torques ($\boldsymbol{\tau}_r \in \mathbb{R}^r$). The end-effector Jacobian of the servicer $\boldsymbol{J}_e = \begin{bmatrix}\boldsymbol{J}_b & \boldsymbol{J}_m & \boldsymbol{0}\end{bmatrix} \in \mathbb{R}^{6\times(6+n+r)}$ maps $\boldsymbol{v}_s$ to the end-effector Cartesian velocity $\boldsymbol{v}_e \in \mathbb{R}^6$. The base Jacobian $\boldsymbol{J}_b \in \mathbb{R}^{6\times6}$ is an invertible adjoint transformation, and $\boldsymbol{J}_m \in \mathbb{R}^{6\times(n+r)}$ is the manipulator Jacobian. The client Jacobian $\boldsymbol{J}_c \in \mathbb{R}^{6\times6}$, is also an invertible adjoint transformation that maps the Cartesian velocity $\boldsymbol{v}_c \in \mathbb{R}^6$ at the client center-of-mass (CoM) to its grasping frame (see Fig. 1). Lastly, $\boldsymbol{F}_c \in \mathbb{R}^6$ is the external wrench acting at the end-effector, which equals the constraint interaction force in the capture phase. For the controller in the approach phase, the dynamics in (1) will be used with $\boldsymbol{F}_c = \boldsymbol{0}$.

The servicer's inertia in (1) has sub-elements of the form

$$\boldsymbol{M}_s = \begin{bmatrix}\boldsymbol{M}_{bb} & \boldsymbol{M}_{bm} & \boldsymbol{M}_{br} \\ \boldsymbol{M}_{bm}^T & \boldsymbol{M}_{mm} & \boldsymbol{0} \\ \boldsymbol{M}_{br}^T & \boldsymbol{0} & \boldsymbol{M}_{rr}\end{bmatrix}, \begin{array}{ll}\boldsymbol{M}_{bb} \in \mathbb{R}^{6\times6} & :\text{base} \\ \boldsymbol{M}_{mm} \in \mathbb{R}^{n\times n} & :\text{manipulator} \\ \boldsymbol{M}_{rr} \in \mathbb{R}^{r\times r} & :\text{wheels}\end{array} \quad (3)$$

and $\boldsymbol{M}_{bm} \in \mathbb{R}^{6\times n}, \boldsymbol{M}_{br} \in \mathbb{R}^{6\times r}$ are the inertia couplings. The structure of (3) will be exploited in the analysis in Sec. III-C2 for redistributing thruster and reaction wheels torques.

Considering a rigid grasp in the post-grasp phase between the servicer's end-effector and the client's grasping interface, the resulting velocity constraint is given by

$$\boldsymbol{v}_e = \boldsymbol{J}_e\boldsymbol{v}_s = \boldsymbol{J}_c\boldsymbol{v}_c. \quad (4)$$

Reformulating the velocity constraint in (4) as $\boldsymbol{A}\begin{bmatrix}\boldsymbol{v}_s^T & \boldsymbol{v}_c^T\end{bmatrix}^T = \boldsymbol{0}$, with $\boldsymbol{A} = \begin{bmatrix}-\boldsymbol{J}_e & \boldsymbol{J}_c\end{bmatrix}$ and using its derivative, we can solve for the constraint forces $\boldsymbol{F}_c$ in (1) and (2) as

$$\boldsymbol{F}_c = \left(\boldsymbol{A}\boldsymbol{M}^{-1}\boldsymbol{A}^T\right)^{-1}\left[\boldsymbol{A}\boldsymbol{M}^{-1}\left(\begin{bmatrix}\boldsymbol{\Gamma} \\ \boldsymbol{0}\end{bmatrix} - \boldsymbol{C}\begin{bmatrix}\boldsymbol{v}_s \\ \boldsymbol{v}_c\end{bmatrix}\right) + \dot{\boldsymbol{A}}\begin{bmatrix}\boldsymbol{v}_s \\ \boldsymbol{v}_c\end{bmatrix}\right] \quad (5)$$

where, $\boldsymbol{M} = \mathrm{diag}(\boldsymbol{M}_s, \boldsymbol{M}_c)$ and $\boldsymbol{C} = \mathrm{diag}(\boldsymbol{C}_s, \boldsymbol{C}_c)$. Note that the term $\boldsymbol{A}\boldsymbol{M}^{-1}\boldsymbol{A}^T$ is invertible since $\boldsymbol{A}$ has full rank as both $\boldsymbol{J}_e$ (due to the $\boldsymbol{J}_b$) and $\boldsymbol{J}_c$ have full row rank. The client velocity in (5) is computed as $\boldsymbol{v}_c = \boldsymbol{J}_c^{-1}\boldsymbol{J}_e\boldsymbol{v}_s$ from (4).

Finally, using (4) we also obtain the dynamics of the combined servicer-client system, see [29], by eliminating $\boldsymbol{F}_c$ from (1) and (2) as

$$\boldsymbol{M}_{sc}(\boldsymbol{q})\dot{\boldsymbol{v}}_s + \boldsymbol{C}_{sc}(\boldsymbol{q}, \dot{\boldsymbol{q}})\boldsymbol{v}_s = \boldsymbol{\Gamma}\ , \quad (6)$$

with, $\boldsymbol{M}_{sc} = \boldsymbol{M}_s + \boldsymbol{J}_e^T\boldsymbol{J}_c^{-T}\boldsymbol{M}_c\boldsymbol{J}_c^{-1}\boldsymbol{J}_e$,

$$\boldsymbol{C}_{sc} = \boldsymbol{C}_s + \boldsymbol{J}_e^T\boldsymbol{J}_c^{-T}\boldsymbol{C}_c\boldsymbol{J}_c^{-1}\boldsymbol{J}_e + \boldsymbol{J}_e^T\boldsymbol{J}_c^{-T}\boldsymbol{M}_c\frac{d}{dt}(\boldsymbol{J}_c^{-1}\boldsymbol{J}_e)\ .$$

Notice that $\boldsymbol{F}_c$ is eliminated in (6) in the post-grasp phase as it only appears as an internal wrench at the grasp point of the combined servicer-client system [30]. For the post-grasp controller, the dynamics in (6) will be used.

It is worth mentioning here that the structure of the inertia matrix presented in (3) also holds for the dynamics in the post-grasp phase in (6), for the combined servicer-client system.

III. Unified Control Framework for Approach Phase and Post-Grasp Phase

In this section, we present the detailed design of the unified control framework in terms of the tasks to be performed to achieve the objectives of the approach and post-grasp phases. (see Table I). We first design a *nominal* controller, meaning, without constraints. Then we analyze its convergence before finally adapting the nominal controller to include constraints.

The objectives of both the approach phase and post-grasp phase are characterized by a primary task and other subtasks (see Table I). Thus, a hierarchical[2] task-based controller can be used. To this end, the control strategy considers a dynamic decoupling through nullspace projections. The control design is unified for both the phases with a primary Cartesian task allocated at the end-effector for client tracking and later, stabilization. The secondary task is unified as a joint-level task on the manipulator to fulfill manipulability and later, configuration safety of the base. Note that the Cartesian and joint task are not in conflict for a floating robot, in contrast with a fixed base robot, as the actuation on the base allows the simultaneous positioning of the end-effector and joint angles. A third task exploits the redundancy in the base actuation to redistribute the control between thrusters and reaction wheels. In summary, the dimension of overall tasks listed in Table I equals the number of DoF of the actuators.

The steps ahead for designing the unified controller for the approach phase and post-grasp phase are summarized below:

i Define task coordinates, followed by nullspace-projected coordinates required to design the decoupled controller.
ii Hierarchically decouple dynamics in nullspace-projected task coordinates to design a nominal impedance controller.
iii Adapt the nominal control inputs in the nullspace-projected task coordinates to account for constraints.

[2]This does not imply sequential but a simultaneous fulfillment of the tasks.

A. Definition of coordinates

The objectives of the approach phase and post-grasp phase are summarized in Table I as tasks to be achieved hierarchically. These can be defined by their task coordinates $\boldsymbol{v}_T$, and corresponding task Jacobian matrices $\boldsymbol{J}_T$ as

$$\begin{matrix}\text{T1:}\\ \text{T2:}\\ \text{T3:}\end{matrix} \underbrace{\begin{bmatrix}\boldsymbol{v}_e\\ \dot{\boldsymbol{q}}_n\\ \dot{\boldsymbol{q}}_r\end{bmatrix}}_{\boldsymbol{v}_T} = \underbrace{\begin{bmatrix}\boldsymbol{J}_e\\ \boldsymbol{J}_n\\ \boldsymbol{J}_r\end{bmatrix}}_{\boldsymbol{J}_T} \boldsymbol{v}_s \quad \text{with} \quad \underbrace{\begin{bmatrix}\boldsymbol{J}_e\\ \boldsymbol{J}_n\\ \boldsymbol{J}_r\end{bmatrix}}_{\boldsymbol{J}_T} = \begin{bmatrix}\boldsymbol{J}_b & \boldsymbol{J}_m & \boldsymbol{0}\\ \boldsymbol{0} & \boldsymbol{I}_n & \boldsymbol{0}\\ \boldsymbol{0} & \boldsymbol{0} & \boldsymbol{I_r}\end{bmatrix}, \quad (7)$$

where, $\boldsymbol{I}_\bullet$ is an identity matrix of dimension $(\bullet \times \bullet)$. The nullspace bases $\boldsymbol{N}_\bullet$ can be deduced from observing the structure in (7) as

$$\begin{aligned}&\text{T2: } \boldsymbol{N}_e^T = \begin{bmatrix}-\boldsymbol{J}_m^T \boldsymbol{J}_b^{-T} & \boldsymbol{I}_n & \boldsymbol{0}\\ \boldsymbol{0} & \boldsymbol{0} & \boldsymbol{I}_r\end{bmatrix} \text{ s.t. } \begin{matrix}\boldsymbol{J}_e \boldsymbol{N}_e = \boldsymbol{0}\\ \begin{bmatrix}\boldsymbol{J}_e\\ \boldsymbol{J}_n\end{bmatrix}\boldsymbol{N}_{en} = \boldsymbol{0}.\end{matrix}\\ &\text{T3: } \boldsymbol{N}_{en}^T = \begin{bmatrix}\boldsymbol{0} & \boldsymbol{0} & \boldsymbol{I}_r\end{bmatrix}\end{aligned} \quad (8)$$

The matrix $\boldsymbol{N}_e$ is the nullspace basis for the end-effector Jacobian, and $\boldsymbol{N}_{en}$ for the end-effector and joints' task Jacobians combined. Note that all nullspaces $\boldsymbol{N}_\bullet^T$ defined in (8) have full row-rank, evident from the identity matrices therein. This means they are well-defined and independent of kinematic singularities of the manipulator related to $\boldsymbol{J}_m$ appearing in (8). Now we redefine the task coordinates $\boldsymbol{v}_T$ in (7) using (8), as projected coordinates $\boldsymbol{v}_N$ with the extended Jacobian matrix $\boldsymbol{J}_N$ (see [31], [32] for details) as

$$\underbrace{\begin{bmatrix}\boldsymbol{v}_e\\ \boldsymbol{v}_n\\ \boldsymbol{v}_r\end{bmatrix}}_{\boldsymbol{v}_N} = \underbrace{\begin{bmatrix}\boldsymbol{J}_e\\ \bar{\boldsymbol{J}}_n\\ \bar{\boldsymbol{J}}_r\end{bmatrix}}_{\boldsymbol{J}_N} \boldsymbol{v}_s \quad \text{where, } \begin{bmatrix}\bar{\boldsymbol{J}}_n\\ \bar{\boldsymbol{J}}_r\end{bmatrix} = \begin{bmatrix}\boldsymbol{J}_n \boldsymbol{N}_e \boldsymbol{N}_e^{M_s+}\\ \boldsymbol{J}_r \boldsymbol{N}_{en} \boldsymbol{N}_{en}^{M_s+}\end{bmatrix} \quad (9)$$
$$\boldsymbol{J}_N^{-1} = \begin{bmatrix}\boldsymbol{J}_e^{M_s+} & \bar{\boldsymbol{J}}_n^{M_s+} & \bar{\boldsymbol{J}}_r^{M_s+}\end{bmatrix}.$$

It is worth mentioning that $\boldsymbol{N}_\bullet \boldsymbol{N}_\bullet^{M_s+} = \boldsymbol{I} - \boldsymbol{J}_\bullet^{M_s+} \boldsymbol{J}_\bullet$, which is a common form of the nullspace projection [33], where,

$$\begin{aligned}\boldsymbol{N}_\bullet^{M_s+} &= (\boldsymbol{N}_\bullet^T \boldsymbol{M}_s \boldsymbol{N}_\bullet)^{-1} \boldsymbol{N}_\bullet^T \boldsymbol{M}_s,\\ \boldsymbol{J}_\bullet^{M_s+} &= \boldsymbol{M}_s^{-1} \boldsymbol{J}_\bullet^T (\boldsymbol{J}_\bullet \boldsymbol{M}_s^{-1} \boldsymbol{J}_\bullet^T)^{-1}.\end{aligned} \quad (10)$$

Notice here that regardless of the approach phase or post-grasp phase, the dynamically consistent nullspaces depend only on $\boldsymbol{M}_s$, and not on $\boldsymbol{M}_c$. This can be shown since $\boldsymbol{N}_\bullet^T \boldsymbol{M}_{sc} = \boldsymbol{N}_\bullet^T \boldsymbol{M}_s$ in (6) using the property $\boldsymbol{N}_\bullet^T \boldsymbol{J}_e^T = \boldsymbol{0}$. This is consistent with the load-independence property of nullspaces [34]. Thus, (9) implies that $\boldsymbol{v}_n$ for task T2 is defined in the nullspace of $\boldsymbol{v}_e$, while $\boldsymbol{v}_r$ for task T3 is in the nullspace of $\boldsymbol{v}_e$ and $\boldsymbol{v}_n$.

B. Dynamic decoupling and nominal control design

Designing the control inputs in the nullspace-projected coordinates in (9) will ensure the desired prioritization. In order to do this, we transform (1) for approach phase (or (6) for post-grasp), using (9) to get

$$\underbrace{\begin{bmatrix}\boldsymbol{\Lambda}_{ee} & \boldsymbol{0} & \boldsymbol{0}\\ \boldsymbol{0} & \boldsymbol{\Lambda}_{nn} & \boldsymbol{0}\\ \boldsymbol{0} & \boldsymbol{0} & \boldsymbol{\Lambda}_{rr}\end{bmatrix}}_{\boldsymbol{\Lambda}} \underbrace{\begin{bmatrix}\dot{\boldsymbol{v}}_e\\ \dot{\boldsymbol{v}}_n\\ \dot{\boldsymbol{v}}_r\end{bmatrix}}_{\dot{\boldsymbol{v}}_N} + \underbrace{\begin{bmatrix}\boldsymbol{\mu}_{ee} & \boldsymbol{\mu}_{en} & \boldsymbol{\mu}_{er}\\ \boldsymbol{\mu}_{ne} & \boldsymbol{\mu}_{nn} & \boldsymbol{\mu}_{nr}\\ \boldsymbol{\mu}_{re} & \boldsymbol{\mu}_{rn} & \boldsymbol{\mu}_{rr}\end{bmatrix}}_{\boldsymbol{\mu}} \underbrace{\begin{bmatrix}\boldsymbol{v}_e\\ \boldsymbol{v}_n\\ \boldsymbol{v}_r\end{bmatrix}}_{\boldsymbol{v}_N} = \underbrace{\begin{bmatrix}\boldsymbol{F}_e\\ \boldsymbol{F}_n\\ \boldsymbol{F}_r\end{bmatrix}}_{\boldsymbol{F}},$$

$$\boldsymbol{\Lambda} = \boldsymbol{J}_N^{-T} \boldsymbol{M}_\bullet \boldsymbol{J}_N^{-1}, \qquad \boldsymbol{F} = \boldsymbol{J}_N^{-T} \boldsymbol{\Gamma}$$
$$\boldsymbol{\mu} = \boldsymbol{J}_N^{-T} \boldsymbol{M}_\bullet \frac{d}{dt}(\boldsymbol{J}_N^{-1}) + \boldsymbol{J}_N^{-T} \boldsymbol{C}_\bullet \boldsymbol{J}_N^{-1}. \quad (11)$$

Here $\bullet$ adapts to the dynamic parameters of the approach phase and post-grasp phase in (1) and (6), respectively. We see that the dynamics in nullspace-projected coordinates in (11), although inertially decoupled, still have Coriolis couplings. To ensure the decoupling of tasks we first compensate for the Coriolis couplings by choosing

$$\boldsymbol{F} = \boldsymbol{F}' + (\boldsymbol{\mu} - \bar{\boldsymbol{\mu}}) \boldsymbol{v}_N, \quad (12)$$

with, $\bar{\boldsymbol{\mu}} = \mathrm{diag}(\boldsymbol{\mu}_{ee}, \boldsymbol{\mu}_{nn}, \boldsymbol{\mu}_{rr})$. The remaining control input to be designed is $\boldsymbol{F}'$. Then (12) in closed loop with (11) results in the following dynamics:

$$\boldsymbol{\Lambda} \dot{\boldsymbol{v}}_N + \bar{\boldsymbol{\mu}} \boldsymbol{v}_N = \boldsymbol{F}'. \quad (13)$$

Note that, compensating purely the Coriolis cross-coupling terms as in (12) is a power-preserving action [35].

To design a control input for tracking a desired time-dependent task trajectory in the nullspace, the projected velocities, $\boldsymbol{v}_N$ are substituted by task velocities, $\boldsymbol{v}_T$ in (13) using the relation $\boldsymbol{v}_N = \boldsymbol{J}_N \boldsymbol{J}_T^{-1} \boldsymbol{v}_T$. This results in the following dynamics:

$$\underbrace{\begin{bmatrix}\boldsymbol{\Lambda}_{ee} & \boldsymbol{0} & \boldsymbol{0}\\ \boldsymbol{\Lambda}_{ne} & \boldsymbol{\Lambda}_{nn} & \boldsymbol{0}\\ \boldsymbol{\Lambda}_{re} & \boldsymbol{\Lambda}_{rn} & \boldsymbol{\Lambda}_{rr}\end{bmatrix}}_{\boldsymbol{\Lambda}'} \underbrace{\begin{bmatrix}\dot{\boldsymbol{v}}_e\\ \ddot{\boldsymbol{q}}_n\\ \ddot{\boldsymbol{q}}_r\end{bmatrix}}_{\dot{\boldsymbol{v}}_T} + \underbrace{\begin{bmatrix}\boldsymbol{\mu}_{ee} & \boldsymbol{0} & \boldsymbol{0}\\ \boldsymbol{\mu}'_{ne} & \boldsymbol{\mu}_{nn} & \boldsymbol{0}\\ \boldsymbol{\mu}'_{re} & \boldsymbol{\mu}'_{rn} & \boldsymbol{\mu}_{rr}\end{bmatrix}}_{\boldsymbol{\mu}'} \underbrace{\begin{bmatrix}\boldsymbol{v}_e\\ \dot{\boldsymbol{q}}_n\\ \dot{\boldsymbol{q}}_r\end{bmatrix}}_{\boldsymbol{v}_T} = \underbrace{\begin{bmatrix}\boldsymbol{F}'_e\\ \boldsymbol{F}'_n\\ \boldsymbol{F}'_r\end{bmatrix}}_{\boldsymbol{F}'},$$

$$\boldsymbol{\Lambda}' = \boldsymbol{\Lambda} \boldsymbol{J}_N \boldsymbol{J}_T^{-1}, \quad \boldsymbol{\mu}' = \bar{\boldsymbol{\mu}} \boldsymbol{J}_N \boldsymbol{J}_T^{-1} + \boldsymbol{\Lambda} \frac{d}{dt}(\boldsymbol{J}_N \boldsymbol{J}_T^{-1}). \quad (14)$$

The sequential transformation to projected task coordinates $\boldsymbol{v}_N$ in (11), followed by the substitution with original task coordinates $\boldsymbol{v}_T$ in (14), reveals how the original task velocities influence the nullspace-projected dynamics [32]. Although the dynamics in projected coordinates $\boldsymbol{v}_N$ in (13) are inertially decoupled, the dynamics viewed from the task coordinates $\boldsymbol{v}_T$ in (14) have a top-down coupling. This is observed from the lower-triangular form of the dynamics in (14). Thus, we see that the lower-priority tasks do not influence the higher-priority ones. This is exploited in the proposed control design to achieve the objectives listed in Table I.

The dynamics in (14) can be used to design a tracking controller for the desired task trajectories in the nullspace. We design a nominal control $\boldsymbol{F}'$ in nullspace-projected task coordinates as follows,

$$\underbrace{\begin{bmatrix}\boldsymbol{F}'_e\\ \boldsymbol{F}'_n\\ \boldsymbol{F}'_r\end{bmatrix}}_{\boldsymbol{F}'} = \boldsymbol{\Lambda}' \begin{bmatrix}\dot{\boldsymbol{v}}_e^d\\ \ddot{\boldsymbol{q}}_n^d\\ \boldsymbol{0}\end{bmatrix} + \boldsymbol{\mu}' \begin{bmatrix}\boldsymbol{v}_e^d\\ \dot{\boldsymbol{q}}_n^d\\ \boldsymbol{0}\end{bmatrix} + \begin{bmatrix}\boldsymbol{E}\boldsymbol{K}_{Pe} \Delta \boldsymbol{x}_e + \boldsymbol{K}_{De} \Delta \boldsymbol{v}_e\\ \boldsymbol{K}_{Pn} \Delta \boldsymbol{q}_n + \boldsymbol{K}_{Dn} \Delta \dot{\boldsymbol{q}}_n\\ \boldsymbol{0}\end{bmatrix} \quad (15)$$

Here $\boldsymbol{v}_e^d$ is the desired Cartesian end-effector velocity and $\Delta \boldsymbol{v}_e = \boldsymbol{v}_e^d - \boldsymbol{v}_e$ is the velocity error. The end-effector's pose error is $\Delta \boldsymbol{x}_e = \begin{bmatrix}\Delta \boldsymbol{x}^T & \Delta \boldsymbol{\epsilon}^T\end{bmatrix}^T \in \mathbb{R}^6$ with position error, $\Delta \boldsymbol{x}$ and the vector part of the quaternion error, $\Delta \boldsymbol{\epsilon}$. The matrix $\boldsymbol{E} = \mathrm{diag}(\boldsymbol{I}_3, \Delta\eta \boldsymbol{I}_3 + \boldsymbol{S}(\Delta \boldsymbol{\epsilon}))$, where, $\Delta\eta$ is the scalar part of the quaternion error and $\boldsymbol{S}(\cdot)$ is the skew-symmetric cross-product operator [36]. Further, $\boldsymbol{q}_n^d, \dot{\boldsymbol{q}}_n^d$ are the desired joint

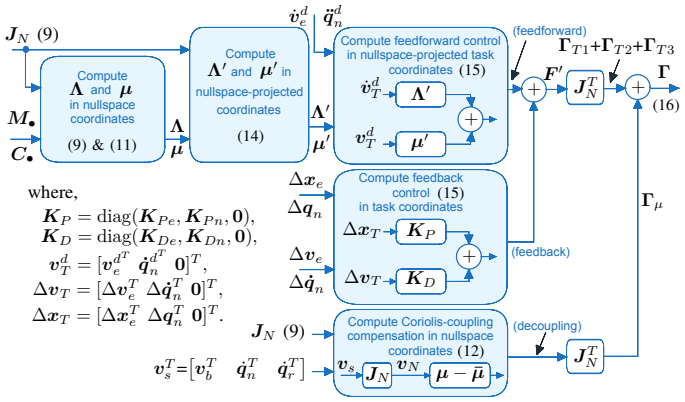

Fig. 3: Block diagram showing the sequence of computations for dynamic decoupling, to arrive at the hierarchical controller in (16).

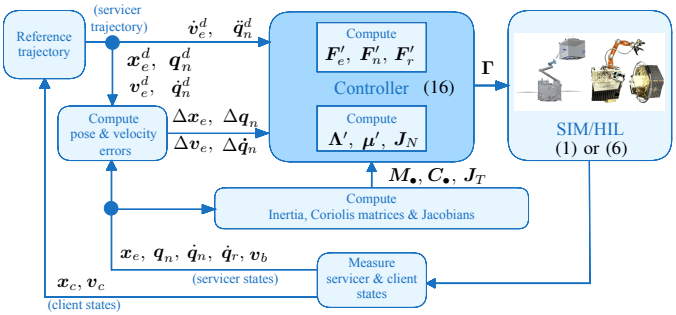

Fig. 4: Overview of the controller (16), detailed in Fig. 3, in closed loop with the dynamics (1) and (6) of the servicer-client system.

position and velocity, $\Delta\boldsymbol{q}_n = \boldsymbol{q}_n^d - \boldsymbol{q}_n$ and $\Delta\dot{\boldsymbol{q}}_n = \dot{\boldsymbol{q}}_n^d - \dot{\boldsymbol{q}}_n$. The proportional-derivative gains for the end-effector and joints are $\boldsymbol{K}_{Pe}, \boldsymbol{K}_{De} \in \mathbb{R}^{6\times6}$ and $\boldsymbol{K}_{Pn}, \boldsymbol{K}_{Dn} \in \mathbb{R}^{n\times n}$, respectively.

Thus, the control $\boldsymbol{F}_e'$ in (16) tracks an end-effector trajectory, while $\boldsymbol{F}_n'$ tracks a joint-level trajectory in accordance with the objectives defined in Table I for T1 and T2. Notice that for the nominal control in (15), $\boldsymbol{F}_r'$ does not track an explicit trajectory because the desired task (T3 in Table I) does not have position tracking requirements. The convergence implications are discussed in the section ahead.

The corresponding nominal control $\boldsymbol{\Gamma}$ input to the servicer in (1) and (6) is obtained from the Jacobian-transpose relation in (11), expanded using (9) as

$$\boldsymbol{\Gamma} = \underbrace{\boldsymbol{J}_e^T\boldsymbol{F}_e'}_{\boldsymbol{\Gamma}_{T1}} + \underbrace{\bar{\boldsymbol{J}}_n^T\boldsymbol{F}_n'}_{\boldsymbol{\Gamma}_{T2}} + \underbrace{\bar{\boldsymbol{J}}_r^T\boldsymbol{F}_r'}_{\boldsymbol{\Gamma}_{T3}} + \boldsymbol{\Gamma}_\mu, \tag{16}$$

where, $\boldsymbol{\Gamma}_\mu = \boldsymbol{J}_N^T(\boldsymbol{\mu} - \bar{\boldsymbol{\mu}})\boldsymbol{v}_N$ is the Coriolis decoupling term and $\boldsymbol{\Gamma}_{T\bullet}$ are related to the three tasks. This concludes the design of the nominal controller (i.e. excluding constraints) for the approach phase and post-grasp phase.

The block diagram in Fig. 3 summarizes the sequence of computations for dynamic decoupling starting from (7) to obtain the final control input to the system in (16). Finally, Fig. 4 gives a broader overview of the control (16) in closed loop with the dynamics (1) and (6) of the servicer-client system, along with the measured states and desired trajectories. Sec. III-C will address the interaction force limit in T1 and actuator limits in T3.

Convergence of the controller: We see from (15) that for tasks T1 and T2, the reaction wheels are redundant DoF, i.e. T1 and T2 can be fulfilled even without reaction wheels. Therefore, the convergence analysis is split into two parts. First we analyse the convergence of the tracking controller for tasks T1 and T2 under the condition that the reaction wheels are not used, i.e., they are locked and task T3 can be omitted. Second, we extend the analysis considering the use of reaction wheels including task T3, for the regulation case, in which regime the controller is operated for the final stabilization phase. The analysis is based on stability theorems for time-varying systems using semi-definite Lyapunov functions [37].

We assume the desired trajectories for all tasks are bounded, and, for the first stage of the analysis, the reaction wheels are locked. The stability analysis is done in a bottom-up approach similar to [32]. Consider the semi-definite Lyapunov function V_2 for task T2 in the set where the errors of states of T1 are zero ($\Delta\boldsymbol{v}_e, \Delta\boldsymbol{x}_e = \boldsymbol{0}$):

$$V_2 = \frac{1}{2}\begin{bmatrix}\Delta\dot{\boldsymbol{q}}_n\\ \Delta\boldsymbol{q}_n\end{bmatrix}^T\begin{bmatrix}\boldsymbol{\Lambda}_{nn} & \varepsilon_n\boldsymbol{\Lambda}_{nn}^T\\ \varepsilon_n\boldsymbol{\Lambda}_{nn} & \boldsymbol{K}_{Pn}\end{bmatrix}\begin{bmatrix}\Delta\dot{\boldsymbol{q}}_n\\ \Delta\boldsymbol{q}_n\end{bmatrix}. \tag{17}$$

where, ε_n is a small non-negative scalar. With $\boldsymbol{F}_n'$ in (15) and $\varepsilon_n = 0$, $\dot{V}_2 = -\Delta\dot{\boldsymbol{q}}_n^T\boldsymbol{K}_{Dn}\Delta\dot{\boldsymbol{q}}_n$. This shows boundedness of involved states in the considered set. Given this boundedness, for $\varepsilon_n > 0$, $\dot{V}_2$ results as follows:

$$-\begin{bmatrix}\Delta\dot{\boldsymbol{q}}_n\\ \Delta\boldsymbol{q}_n\end{bmatrix}^T\begin{bmatrix}\boldsymbol{K}_{Dn} - \varepsilon_n\boldsymbol{\Lambda}_{nn} & \frac{1}{2}\varepsilon_n(\boldsymbol{K}_{Dn} - \boldsymbol{\mu}_{nn}^T)^T\\ \frac{1}{2}\varepsilon_n(\boldsymbol{K}_{Dn} - \boldsymbol{\mu}_{nn}^T) & \varepsilon_n\boldsymbol{K}_{Pn}\end{bmatrix}\begin{bmatrix}\Delta\dot{\boldsymbol{q}}_n\\ \Delta\boldsymbol{q}_n\end{bmatrix}.$$

This can further be shown to be negative-definite, for a sufficiently small $\varepsilon_n > 0$. This implies the states of T2 are uniformly asymptotically stable in the set where errors of states of T1 are zero.

Further, consider the following semi-definite Lyapunov function V_1 for task T1:

$$V_1 = \frac{1}{2}\begin{bmatrix}\Delta\boldsymbol{v}_e\\ \Delta\boldsymbol{x}_e\end{bmatrix}^T\begin{bmatrix}\boldsymbol{\Lambda}_{ee} & \varepsilon_e\boldsymbol{\Lambda}_{ee}^T\\ \varepsilon_e\boldsymbol{\Lambda}_{ee} & \boldsymbol{K}_{Pe}\end{bmatrix}\begin{bmatrix}\Delta\boldsymbol{v}_e\\ \Delta\boldsymbol{x}_e\end{bmatrix}. \tag{18}$$

where, ε_e is a small non-negative scalar. With $\boldsymbol{F}_e'$ in (15) and $\varepsilon_e = 0$, $\dot{V}_1 = -\Delta\boldsymbol{v}_e^T\boldsymbol{K}_{De}\Delta\boldsymbol{v}_e$. This shows boundedness of all involved states, cascaded with the boundedness of states in the set where T1 errors are zero. Given boundedness, for a sufficiently small $\varepsilon_e > 0$, $\dot{V}_1$ can be shown to be negative-definite similar to the line of argumentation for $\dot{V}_2$ above. Invoking the stability theorem for time-varying systems using semi-definite Lyapunov functions [37], the negative-definiteness of $\dot{V}_1$ and $\dot{V}_2$ allows to conclude the equilibrium $(\Delta\boldsymbol{v}_e, \Delta\boldsymbol{x}_e, \Delta\dot{\boldsymbol{q}}_n, \Delta\boldsymbol{q}_n = \boldsymbol{0})$ to be uniformly asymptotically stable. Note that the convergence of joint errors in task T2 (in the nullspace of the end-effector) is independent of manipulator singularities. This is due to the nullspaces in (8) being well-defined for the fully-actuated (6-DoF) base that compensates for any loss of DoF due to singularities (see [21] for details). The proof of stability here does not imply sequential convergence, rather it is a simultaneous convergence of hierarchical tasks.

For the second stage of the analysis, we assume the reaction wheels are unlocked and include the task T3. As task T3 is the lowest in the hierarchy, consider the candidate Lyapunov function $V_3 = \dot{\boldsymbol{q}}_r^T \boldsymbol{\Lambda}_r \dot{\boldsymbol{q}}_r$ in the set where errors of states of T1 and T2 are zero ($\Delta \boldsymbol{v}_e, \Delta \boldsymbol{x}_e, \Delta \boldsymbol{q}_n, \Delta \dot{\boldsymbol{q}}_n = \boldsymbol{0}$). Note here that $\boldsymbol{q}_r$ is not a relevant state of the system since the angular position of the rotationally symmetric reaction wheels does not influence the inertia in (1) or (6). Under the regulation case for tasks T1 and T2, the nominal $\boldsymbol{F}_r'$ in (15) leads to $\dot{V}_3 = 0$ in the considered set. This shows that the reaction wheels converge to a constant residual velocity in the nullspace at the end of the stabilization phase. This is desired by design as, the reaction wheels, unlike a manipulator link, are actuators that work on the principle of exchanging momentum between the base to produce torques. The wheel velocities are not damped, as this would result in the use of thrusters for damping the wheels in order to balance the control torque requirements of tasks T1 and T2. This defeats the purpose of using reaction wheels. For the tracking case in the approach phase, trajectories with bounded velocities for tasks T1 and T2 ensure bounded velocities of the reaction wheels.

C. Adapting nominal controller to include constraints

The nominal controller in (16) does not guarantee respecting interaction force limits or thruster limits, dictated by space mission requirements. In the following we see how the nominal controller can be adapted to meet these requirements.

1) Optimizing $\boldsymbol{F}_e'$ for interaction force limits in the post-grasp phase: Analysing the influence of the control effort $\boldsymbol{\Gamma}$ from (16), on the interaction forces $\boldsymbol{F}_c$ at the end-effector in (5), we observe the terms $\boldsymbol{\Gamma}_{T2}$ and $\boldsymbol{\Gamma}_{T3}$ have zero influence on $\boldsymbol{F_c}$. This can be proven by plugging in $\boldsymbol{\Gamma}_{T2}, \boldsymbol{\Gamma}_{T3}$ in (5) and using the property of dynamic consistency, $\boldsymbol{J}_e \boldsymbol{M}_{sc}^{-1} \boldsymbol{N}_{\bullet}^{T+} = \boldsymbol{0}$. This is because they lie in the dynamically consistent nullspace of the end-effector task. This also demonstrates the advantage of designing the secondary tasks such as the joint reconfiguration in the nullspace, as it has no influence on the interaction forces during stabilization. Finally, substituting $\boldsymbol{\Gamma}$ from (16) into (5) gives us the relation between $\boldsymbol{F}_e'$ and $\boldsymbol{F}_c$ as

$$\boldsymbol{F_c} = (\boldsymbol{I} + \boldsymbol{\Lambda}_{ee} \boldsymbol{\Lambda}_{cc}^{-1})^{-1} \boldsymbol{F}_e' + \boldsymbol{f}(\boldsymbol{v}_s, \boldsymbol{v}_c), \tag{19}$$

$$\text{where, } \boldsymbol{\Lambda}_{cc} = (\boldsymbol{J}_c \boldsymbol{M}_c^{-1} \boldsymbol{J}_c^T)^{-1}, \quad \boldsymbol{\Lambda}_{ee} = (\boldsymbol{J}_e \boldsymbol{M}_s^{-1} \boldsymbol{J}_e^T)^{-1}.$$

The quantities $\boldsymbol{\Lambda}_{cc}, \boldsymbol{\Lambda}_{ee} \in \mathbb{R}^{6\times 6}$ describe the Cartesian inertia of the client and servicer at the end-effector, respectively. For brevity, the remaining terms in (5) arising from Coriolis/centrifugal effects are depicted as $\boldsymbol{f}(\boldsymbol{v}_s, \boldsymbol{v}_c)$ in (19). Thus, (19) shows us that the interaction force $\boldsymbol{F}_c$ is dominated by $\boldsymbol{F}_e'$ scaled by the ratio of the Cartesian inertia of the servicer and client at the end-effector. Typically $\boldsymbol{\Lambda}_{cc} \gg \boldsymbol{\Lambda}_{ee}$, which is counter-intuitive since the client satellite is lighter than the servicer (base plus arm). The right intuition lies in observing that $\boldsymbol{\Lambda}_{ee}$, is dictated by the manipulability of the arm (i.e. the inertia of the arm rather than the base). On the contrary, $\boldsymbol{\Lambda}_{cc}$ is a large inertia at the end-effector, due to the client's rigid-body mass, which is typically heavier than the manipulator arm. This leads to a first-order approximation of (19) as $\boldsymbol{F}_c \approx \boldsymbol{F}_e'$ while also neglecting $\boldsymbol{f}(\boldsymbol{v}_s, \boldsymbol{v}_c)$ for slow motions.

Further, stabilization is to be performed as a regulation task to remove the spin of the combined servicer-client system, which implies $\boldsymbol{v}_e^d = \boldsymbol{0}$. Thus, to limit the interaction forces the optimization of $\boldsymbol{F}_e'$ is formulated as the following QP problem:

$$\min_{\boldsymbol{F}_e^*} \quad \frac{1}{2} (\boldsymbol{F}_e^* - \boldsymbol{F}_e')^T \boldsymbol{Q}_c (\boldsymbol{F}_e^* - \boldsymbol{F}_e') \tag{20}$$

$$\text{s.t. } |\boldsymbol{F}_c|_i \leq \boldsymbol{F}_{c,max_i} \tag{21}$$

$$\boldsymbol{v}_e^T (\boldsymbol{F}_e^* - \boldsymbol{E}\boldsymbol{K}_{Pe} \Delta \boldsymbol{x}_e) < 0, \tag{22}$$

with, the weighting matrix, $\boldsymbol{Q}_c \in \mathbb{R}^{6\times 6}$, and $\boldsymbol{F}_e^*$ is the optimized control wrench.

The constraint (21) limits the interaction forces, according to space mission requirements, where, $\boldsymbol{F}_{c,max_i}$ is the component-wise threshold of the allowable maximum interaction wrench. The constraint (22) ensures that the stability requirements are met by the optimized wrench. Taking the time-derivative of the candidate Lyapunov function V_1 in (18) with $\varepsilon_e = 0$ for the regulation case, the constraint is obtained by imposing that $\dot{V}_1$ is negative-definite to ensure boundedness. Finally, $\boldsymbol{F}_e^*$ replaces $\boldsymbol{F}_e'$ in (16) and Fig. 4.

2) Optimizing $\boldsymbol{F}_r'$ for thruster capacity limits: We know that $\boldsymbol{F}_r'$ maps to the actuation $\boldsymbol{\Gamma}_{T3}$ on the servicer through the Jacobian-transpose $\bar{\boldsymbol{J}}_r^T$ as seen in (16). A closer look at $\bar{\boldsymbol{J}}_r$ using the definition in (9) and the structure of the inertia matrix in (3) reveals

$$\bar{\boldsymbol{J}}_r = \begin{bmatrix} \boldsymbol{M}_{rr}^{-1} \boldsymbol{M}_{br}^T & \boldsymbol{0} & \boldsymbol{I}_r \end{bmatrix} \tag{23}$$

with, $\boldsymbol{M}_{br}^T = \begin{bmatrix} \boldsymbol{0} & \boldsymbol{M}_{\omega r}^T \end{bmatrix}$. Here $\boldsymbol{M}_{\omega r}$ is the inertia coupling of reaction wheels to the base's angular velocity. From (23) and through $\boldsymbol{\Gamma}_{T3} = \bar{\boldsymbol{J}}_r^T \boldsymbol{F}_r'$ we observe that $\boldsymbol{F}_r'$ cannot influence the linear force on the base or the manipulator torques. However, the base torques can be modified by redesigning $\boldsymbol{F}_r'$. The optimization of $\boldsymbol{F}_r'$ [23] is formulated as a QP problem:

$$\min_{\boldsymbol{F}_r^*} \quad \frac{1}{2} (\bar{\boldsymbol{\Gamma}} + \bar{\boldsymbol{J}}_r^T \boldsymbol{F}_r^*)^T \boldsymbol{Q}_\Gamma (\bar{\boldsymbol{\Gamma}} + \bar{\boldsymbol{J}}_r^T \boldsymbol{F}_r^*) \tag{24}$$

$$\text{s.t. } |\boldsymbol{\tau}_b|_i \leq \boldsymbol{\tau}_{b,max_i}. \tag{25}$$

In the approach phase, $\bar{\boldsymbol{\Gamma}} = \boldsymbol{\Gamma}_{T1} + \boldsymbol{\Gamma}_{T2} + \boldsymbol{\Gamma}_\mu$ from (16). In the post-grasp phase, $\bar{\boldsymbol{\Gamma}} = \boldsymbol{\Gamma}_{T1}^* + \boldsymbol{\Gamma}_{T2} + \boldsymbol{\Gamma}_\mu$, which includes the optimized end-effector wrench from (20) for limiting interaction forces with $\boldsymbol{\Gamma}_{T1}^* = \boldsymbol{J}_e^T \boldsymbol{F}_e^*$. Notice how the formulation in (24) limits the dimension of optimization to the redundant DoFs as compared to all system DoFs in [23].

The cost function in (24) penalizes the actuation according to the weighting matrix $\boldsymbol{Q}_\Gamma \in \mathbb{R}^{(6+n+r)\times(6+n+r)}$. The constraint (25) limits the final torques distributed to thrusters, $\boldsymbol{\tau_b}$. Here $\boldsymbol{\tau}_{b,max_i}$ is the component-wise, threshold of the allowable maximum thruster torque, dictated by thruster limits. The term $\boldsymbol{F}_r^*$ is the optimized variable that reallocates torques between the thrusters and reaction wheels. Hence, $\boldsymbol{F}_r^*$ replaces $\boldsymbol{F}_r'$ in (16) and Fig. 4. By tuning the weights appropriately, the torque distribution can be adapted to the requirements of the phase of operation. The optimized result does not alter the convergence analysis since, in the set where tasks T1 and T2 is converged, $\boldsymbol{F}_r^* = \boldsymbol{0}$ for the regulation case at the end of the post-grasp phase.

Finally, the algorithm ahead, to compute the unified control law, complements the block diagrams in Fig. 3 and Fig. 4.

Algorithm Computing Unified Control Law

Require: Kinematics ($\boldsymbol{J}_e, \boldsymbol{J}_c$) and dynamics ($\boldsymbol{M}_\bullet, \boldsymbol{C}_\bullet$) from (1),(6) in generalized coordinates
1: Compute kinematics ($\boldsymbol{J}_N$ from (9)) and dynamics ($\boldsymbol{\Lambda}, \boldsymbol{\mu}$ from (11)) in nullspace coordinates
2: Compute Coriolis decoupling $(\boldsymbol{\mu} - \bar{\boldsymbol{\mu}})\boldsymbol{v}_N$ from (12)
3: Compute dynamics ($\boldsymbol{\Lambda}', \boldsymbol{\mu}'$ from (14)) in nullspace-projected task coordinates
4: Compute nominal control law $\boldsymbol{F}'$, $\boldsymbol{\Gamma}$ from (15), (16)
5: **if** phase = post-grasp **then**
6: Optimize end-effector wrench ($\boldsymbol{F}_e^*$ from (20)-(22)) for limiting interaction forces
7: **end if**
8: Optimize torque distribution between reaction wheels and thrusters ($\boldsymbol{F}_r^*$ from (24)-(25))
9: Compute optimized control law in actuator coordinates (replace $\boldsymbol{F}_e', \boldsymbol{F}_r'$ with $\boldsymbol{F}_e^*, \boldsymbol{F}_r^*$ in (16))

IV. VALIDATION

This section presents the validation of the proposed control strategy using two setups – i) simulation (SIM) using the EROSS IOD [40] mission setup and, ii) hardware-in-the-loop (HIL) experiments using the COMRADE [3] mission setup on the OOS-Sim at DLR [24]. Both setups are shown in Fig. 1. The dynamic, kinematic and control parameters for the SIM and HIL setups are summarized in Table II.

The controller gains are adapted to the desired performance in tracking (for approach phase) and compliance (for post-grasp phase). Initial estimates of the gains are obtained from a frequency-domain analysis using the linearized closed-loop dynamics about the initial and final configurations of the servicer[3]. The controller gains from the approach to grasp phase are updated to be more compliant to impact, yet more dissipative for stabilization.

The SIM setup uses the Open Dynamics Engine [41] in CoppeliaSim for simulating the servicer and client dynamics. The manipulator used in simulation is the CAESAR space robot [39], a 7-DoF redundant robot. The grasping dynamics between manipulator's end-effector and capture point is modeled as a plastic contact. A force-torque sensor at the end-effector measures the interaction forces as ground truth.

The HIL setup uses the OOS-Sim facility – a platform for 6-DoF zero-gravity dynamics validation. It uses two industrial robots to emulate the motion of the floating servicer and client satellites, computed using a model-based floating-dynamics [42]. The servicer satellite is equipped with a 7-DoF redundant Light-Weight-Robot (LWR) that is torque-controlled at 1kHz. A force-torque sensor on the client is used to measure and transmit the real contact dynamics on the servicer during the post-grasp phase. This is also used as ground truth, for validating the interaction force limitation. The torque distribution to reaction wheels is simulated while considering its dynamics parameters. The first-order approximation of the interaction force in (5) is used to limit post-grasp forces in the experiment.

[3]As the impedance gains are only relevant to tasks T1 and T2, the linearization for the sake of gain tuning can be simplified by eliminating task T3 on the redundant reaction wheels. The initial gains can thus be tuned against step responses for tracking performance, and against impulse responses for compliance performance. These estimates form the basis for further tuning and validation in a nonlinear dynamic environment.

TABLE II: SIM and HIL setup parameters. *Principal Moment of Inertia (MOI), **Orientation as Euler angles in XYZ convention, †Double-Diagonalization (DD) [38] with damping ratio 0.7, $^{\dagger\dagger}Q_\Gamma$=diag$(0_3, Q_{\tau_b}, 0_n, Q_{\tau_r})$, $^\#$Order of magnitudes as in [17].

DYNAMIC/KINEMATIC PARAMETERS			
Parameter		**SIM**	**HIL**
Client mass & MOI*		350kg, $(58.33, 58.33, 58.33)$kg m^2	400kg, $(360, 362.95, 264.94)$kg m^2
Servicer mass & MOI*		360kg, $(210.9, 77.9, 212.1)$kg m^2	1000kg, $(700, 600, 500)$kg m^2
Number of reaction wheels		4	3
Manipulator arm		7-DoF CAESAR robot [39]	7-DoF Light Weight Robot (LWR)
Initial joint angles		$(90, 60, 0, 132, 90, -90, 50)$deg	$(-6.64, 13.26, 3.75, 90.56, 2.35, -54.18, -3.39)$deg
Initial end-effector pose**		$(0.84, -0.30, 1.65)$m, $(62, 0, 90)$deg	$(1.27, -0.01, 0.89)$m, $(-173, 53, -175)$deg
Initial client grasp pose**		$(0.95, -0.91, 2.16)$m, $(90, 5, 90)$deg	$(1.33, -0.41, 0.47)$m, $(-136, 47, -178)$deg
Initial client velocity norm		2.865deg s^{-1}	0.5deg s^{-1}
CONTROLLER PARAMETERS			
Setup	**Task**	**Gains/ Weights**	**Approach phase**	**Post-Grasp phase**
SIM	T1	K_{Pe}	diag([250, 250, 250]N m^{-1}, [50, 50, 50]N m rad^{-1})	diag([10, 10, 10]N m^{-1}, [5, 5, 5]N m rad^{-1})
		K_{De}	diag([200, 200, 200]N m^{-1}s, [125, 125, 125]N m rad^{-1}s)	diag([400, 400, 400]N m^{-1}s, [250, 250, 250]N m rad^{-1}s)
		Q_c	-	diag($1/F_{c,max_i}^2$), $F_{c,max_i}^\#$=([10, 10, 10]N, [7, 7, 7]N m)
	T2	K_{Pq}	diag(120, 120, 100, 100, 50, 40, 40)N m rad^{-1}	diag(120, 120, 100, 100, 50, 40, 40)N m rad^{-1}
		K_{Dq}	variable damping using DD †	DD † scaled by diag(5, 5, 5, 10, 25, 12.5, 22.5)
	T3	$Q_\Gamma^{\dagger\dagger}$	Q_{τ_b}=I_3, Q_{τ_r}=0_r, τ_{b,max_i}=15N m	Q_{τ_b}=0_3, Q_{τ_r}=I_r, τ_{b,max_i}=15N m
HIL	T1	K_{Pe}	diag([700, 500, 500]N m^{-1}, [40, 60, 40]N m rad^{-1})	diag([50, 50, 50]N m^{-1}, [30, 30, 30]N m rad^{-1})
		K_{De}	diag([100, 100, 100]N m^{-1}s, [24, 24, 24]N m rad^{-1}s)	diag([100, 100, 100]N m^{-1}s, [24, 24, 24]N m rad^{-1}s)
		Q_c	-	diag($1/F_{c,max_i}^2$), $F_{c,max_i}^\#$=([12, 12, 12]N, [8, 8, 8]N m)
	T2	K_{Pq}	diag(60, 60, 60, 40, 35, 25, 30)N m rad^{-1}	diag(2, 30, 1, 10, 1, 10, 0.5)N m rad^{-1}
		K_{Dq}	variable damping using DD †	diag(20, 60, 10, 60, 10, 60, 7)N m rad^{-1}s
	T3	$Q_\Gamma^{\dagger\dagger}$	Q_{τ_b}=I_3, Q_{τ_r}=0_r, τ_{b,max_i}=15N m	Q_{τ_b}=0_3, Q_{τ_r}=I_r, τ_{b,max_i}=15N m

The SIM and HIL results are summarized graphically in Fig. 5 and quantitatively in Table III, validating the proposed control objectives in Table I. Snapshots visualizing the SIM and HIL scenarios at different stages of the approach and post-grasp stabilization are also provided in Fig. 5. The graphical results in Fig. 5 show the most relevant states, control, and forces recorded for the SIM and HIL experiments. The columns a and b in Fig. 5 show the results of the SIM experiment for the approach and post-grasp phases, respectively, while the columns c and d show the results of the HIL experiment for the approach and post-grasp phases, respectively. The moment of grasp (contact) in SIM and HIL results can be recognized from the characteristic spike at the beginning of the graphs presented for the post-grasp phase.

A. Simulation (SIM) results

The snapshots of the SIM analysis in Fig. 5 (left), show the start of the approach phase, grasp instant, and the end of the post-grasp stabilization. Unlike the problem seen in Fig. 2, here the proposed control strategy is able to approach the spinning client with a safe pose and better manipulability while the end-effector reaches the client grasp. This results in the base sychronizing its spin along with the client, all the while maintaining a safe relative pose. This can be seen by comparing the orientation of the base in the SIM snapshots of the grasp instant versus the approach start in Fig. 5 (left). The post-grasp phase further dissipates the spin of the client with more compliance, yet achieves a safe desirable pose (of manipulator and thus base). This can be seen in the SIM snapshot of the post-grasp end in Fig. 5 (left), where, the servicer reaches a desired pose suited for later manipulation of the stabilized client.

Fig. 5 a.i and a.ii show the end-effector tracking a smooth trajectory to align with the client grasp pose at the end of the approach phase, shown in a.iii and a.iv and highlighted in blue. Fig. 5 b.i and b.ii show the effect of constraints that limit the interaction forces and torques in the post-grasp phase to their respective thresholds. Fig. 5 b.iii and b.iv show the resulting stabilization of the spinning client (initial spin of $2.86\mathrm{deg/s}$) as the linear and angular body velocities get damped. A comparison of the performance of the controller was performed without the QP optimization for interaction forces and it was found that the threshold was violated by 93.8% in force and 65.87% in torque in this scenario.

Fig. 5 a.v shows the tracking of a joint pose in the nullspace to arrive at a manipulable configuration at the end of the approach phase. It is this simultaneous tracking of a joint trajectory in addition to the end-effector pose that results in the base synchronizing its spin to that of the client before capture. Fig. 5 b.v shows the arm stabilizing during the post-grasp phase as the joint velocities get damped.

Fig. 5 a.vi shows the complete redistribution of base torques to the four reaction wheels in the approach phase. On the other hand, Fig. 5 b.vi shows the torque distribution to the thrusters being maximized for damping the acquired momentum in the grasp phase. As shown in Fig. 6, the residual angular momentum corresponds to that stored in the wheels from the approach phase to stabilization under thruster torque limits.

TABLE III: Quantitative metrics for SIM and HIL performance. † Euclidean norm, *Absolute error along any axes, **Time for absolute joint velocity to reach below $0.1\mathrm{deg/s}$ along all axes after grasp.

Performance metric	SIM	HIL
Maximum end-effector position error † (m)	$1.9e{-5}$	$1.1e{-2}$
Maximum end-effector orientation error † (deg)	$2.3e{-2}$	1.5
Maximum joint tracking error* (deg)	$6.7e{-2}$	2.95
Settling time for post-grasp stabilization** (s)	45	43

B. Experimental (HIL) results

Similar to SIM results, the snapshots of the HIL experiments in Fig. 5 (right) show the start of the approach phase, grasp instant, and the end of the post-grasp stabilization. Here again the proposed method leads to the base synchronizing its spin to that of the client in the approach phase, thus bringing the manipulator into a desirable pose for capture. This can be seen by comparing the orientation of the base and the manipulator pose in the HIL snapshots of the grasp instant versus the approach start in Fig. 5 (right).

In particular, unlike the problem seen in Fig. 2, the proposed control strategy is able to safely stabilize the client through the nullspace potential on the manipulator joints, thus avoiding collision between the base and client. This can be seen in the HIL snapshot for the post-grasp end in Fig. 5 (right).

The HIL results in Fig. 5 can be correlated with the SIM results described in Sec. IV-A. Fig. 5 c.i and c.ii show the end-effector tracking and Fig. 5 d.i and d.ii show the interaction forces and torques being limited in the post-grasp phase, while the spinning client (initial spin of $0.5\mathrm{deg/s}$) stabilizes, seen from the body velocities being damped in Fig. 5 d.iii and d.iv.

Fig. 5 c.v. shows the nullspace joint tracking in the approach phase and the joints stabilize in the post-grasp phase, see Fig. 5 d.v. For faster energy dissipation within the workspace limits of the HIL facility, stabilization is performed with an additional damping gain on the base velocity applied in the nullspace of the end-effector task. Further, the stiffness in the post-grasp phase is emphasized on the joints that ensure the safe relative configuration between servicer and client, while the remaining are relaxed to increase compliance during stabilization (see Table II).

Similar to SIM results, Fig. 5 c.vi shows the redistribution of base torques to the three reaction wheels in the approach phase whereas Fig. 5 d.vi shows the maximization of thruster utilization in the post-grasp phase. The activation of the limit on the base thrust can be seen resulting in the co-utilization of reaction wheels. The control input demanded from the servicer in the grasp phase is greater than the approach phase, as expected due to the momentum injected during the grasp of the client satellite. For more tests, see accompanying video[4].

C. Further results and discussion

To analyze the robustness of the controller, we study the sensitivity of the controller to gain variation and to client parameter uncertainties, respectively in simulation. The gain sensitivity analysis is performed by varying the gains from

[4]A supplementary video of the experiments accompanies this manuscript.

Fig. 5: SIM and HIL results showing fulfillment of proposed control objectives in Table I. Results divided as per tasks T1, T2, T3 (rows) for the approach and post-grasp phases (columns). For ease of presentation, Euler angles (ϕ, θ, ψ in the XYZ convention) are reported here.

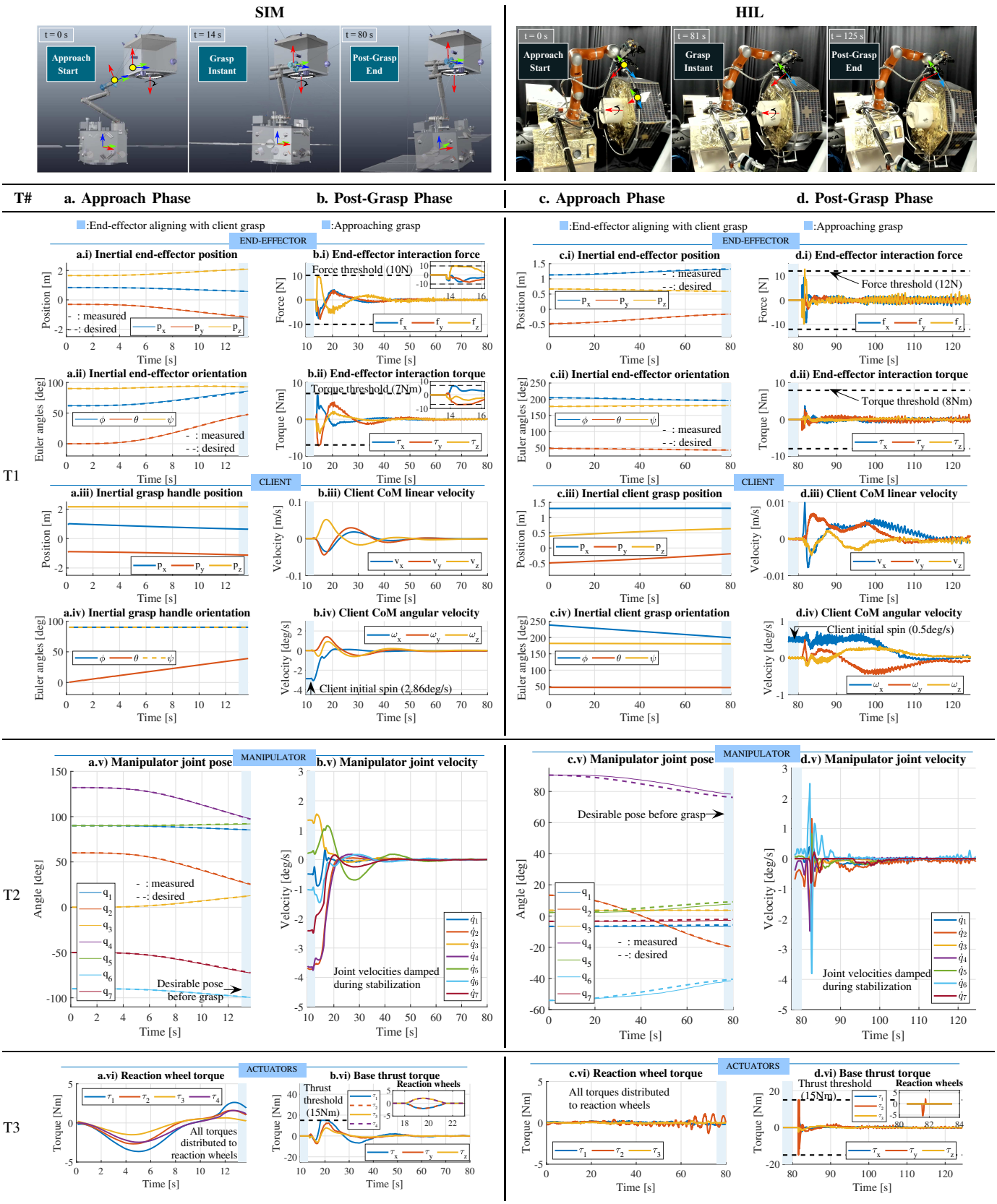

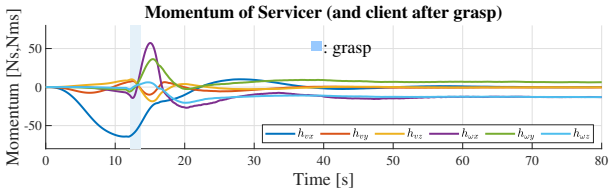

Fig. 6: Momentum of servicer (and client after grasp) for SIM experiment in Fig. 5 (left). Linear momentum damped while residual angular momentum stored in wheels under thruster torque limits.

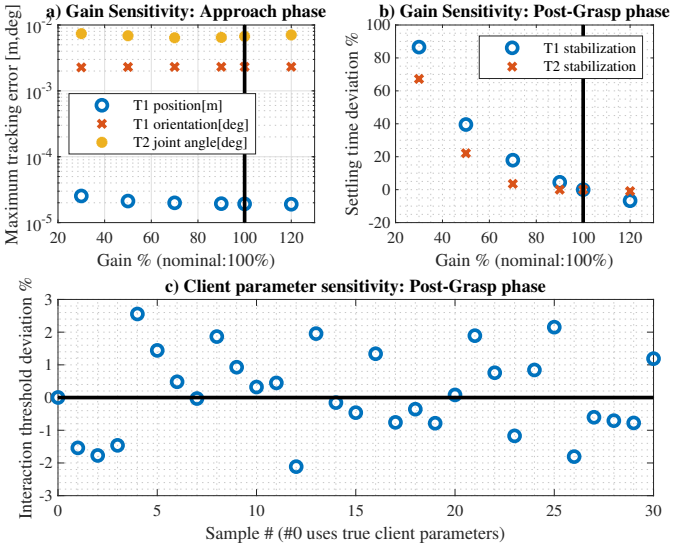

Fig. 7: Parameter sensitivity to control performance.

30% to 120% of the nominal gains (100%) in Table II. Across the gain variations in the approach phase (see Fig. 7 a), we observe that the maximum Euclidean error in end-effector tracking is below 1e-4 m and 1e-2 deg in position and orientation, respectively. Further, the manipulator tracking error about any joint, is below 1e-2 deg. For the post-grasp phase (see Fig. 7 b), the percentage of settling time for stabilization increases (or decreases) with decrease (or increase) in gains.

Robustness is further analyzed considering client parameter uncertainties in the mass, inertia and center-of-mass up to 20% simultaneously. We observe that the violation in the threshold of interaction forces does not exceed 3% (see Fig. 7 c) for the 30 simulations with uniformly distributed samples of client parameter uncertainties. The forces are limited to a higher (or lower) threshold as the optimizer under- (or over-) compensates for the dynamics of the client. Therefore, we evaluated the overall robustness to a wide range of gains and client parameter uncertainties.

The robustness of the controller to client parameter uncertainties is in fact due to the terms $\boldsymbol{\Gamma}_{T1}, \boldsymbol{\Gamma}_{T2}, \boldsymbol{\Gamma}_{T3}$ in (16) being independent of the inertia parameters of the client in the post-grasp phase. This is due to the regulation scheme for T1 and the load-independence of the nullspaces tasks T2 and T3. The only dependency on client parameters is through the Coriolis coupling $\boldsymbol{\Gamma}_{\mu}$ and the optimized $\boldsymbol{F}_e^*$ via the interaction force limitation with (19).

Further, we emphasize the configuration safety achieved in the post-grasp phase evidenced by the result of the HIL experiment in Fig. 5 (right) which mitigated the collision risk shown in Fig. 2 (right). The nullspace potential on the joints responsible for this, not only achieved safety, but also did so while staying decoupled from the interaction forces (see (19)). This highlights the advantage of the hierarchical controller.

Lastly, the unified impedance control allows for continuous operation (approach to stabilization) in compliant mode while only updating the gains for effective stabilization. Further, a unified control simplifies hardware implementation, validation, traceability and troubleshooting.

V. Conclusions

In this paper we proposed a unified control framework for tackling the mission requirements in the approach and grasp/post-grasp phase. The presented method is a hierarchical nullspace projection-based controller that prioritizes the end-effector task of the servicer for tracking and stabilizing the client satellite in the approach and grasp/post-grasp phases, respectively. In the nullspace of the end-effector, a planned joint trajectory is tracked with the support of the base actuation. The method also allowed the modification of terms within the nullspace projection-based control scheme to incorporate mission constraints on interaction forces during the stabilization phase, and thruster torque limits using reaction wheels.

The controller is shown to be convergent for the tasks designed in the three hierarchy levels considering the end-effector, manipulator, and reaction wheels of the servicer. The results of the designed control strategy are presented as both simulation and hardware-in-the-loop experiments. Extension of the method to discretized thrust control on the servicer base may be the scope of future work.

References

[1] D. Henry *et al.*, "Model-based fault diagnosis and tolerant control: the esa's e.deorbit mission," in *2019 18th European Control Conference (ECC)*, 2019, pp. 4356–4361.

[2] P. Rank, Q. Mühlbauer, W. Naumann, and K. Landzettel, "The DEOS automation and robotics payload," in *Symp. on Advanced Space Technologies in Robotics and Automation, ASTRA, the Netherlands*, 2011.

[3] P. Colmenarejo *et al.*, "Results of the comrade project: combined control for robotic spacecraft and manipulator in servicing missions: active debris removal and re-fuelling," in *11th International ESA Conference on Guidance, Navigation & Control Systems*, 2020.

[4] Papadopoulos *et al.*, "Robotic manipulation and capture in space: A survey," *Frontiers in Robotics and AI*, vol. 8, 2021.

[5] S. Jaekel *et al.*, "Design and operational elements of the robotic subsystem for the e.deorbit debris removal mission," *Frontiers in Robotics and AI*, vol. 5, p. 100, 2018.

[6] H. S. Jayakody *et al.*, "Robust adaptive coordination controller for a spacecraft equipped with a robotic manipulator," *Journal of Guidance, Control, and Dynamics*, vol. 39, no. 12, pp. 2699–2711, 2016.

[7] P. Huang *et al.*, "Attitude coordinated control for docked spacecraft based on estimated coupling torque," *Journal of Aerospace Engineering*, vol. 29, no. 6, 2016.

[8] M. De Stefano *et al.*, "Multi-rate tracking control for a space robot on a controlled satellite: A passivity-based strategy," *IEEE Robotics and Automation Letters*, vol. 4, no. 2, pp. 1319–1326, April 2019.

[9] A. Flores-Abad, O. Ma, K. Pham, and S. Ulrich, "A review of space robotics technologies for on-orbit servicing," *Progress in Aerospace Sciences*, vol. 68, pp. 1 – 26, 2014.

[10] M. Alizadeh and G. Zhu, "A comprehensive survey of space robotic manipulators for on-orbit servicing," *Frontiers in robotics and AI*, vol. 11, p. 1470950, 10 2024.

[11] D. Nenchev and K. Yoshida, "Impact analysis and post-impact motion control issues of a free-floating space robot subject to a force impulse," *IEEE Transactions on Robotics and Automation*, vol. 15, no. 3, 1999.
[12] K. Yoshida and H. Nakanishi, "Impedance matching in capturing a satellite by a space robot," in *Proceedings 2003 IEEE/RSJ International Conference on Intelligent Robots and Systems*, vol. 4, 2003.
[13] I. S. Paraskevas and E. G. Papadopoulos, "On the use of the center of percussion for space manipulators during impacts," in *2013 IEEE International Conference on Robotics and Automation*, 2013.
[14] A. M. Giordano, A. Dietrich, C. Ott, and A. Albu-Schäffer, "Coordination of thrusters, reaction wheels, and arm in orbital robots," *Robotics and Autonomous Systems*, vol. 131, p. 103564, 2020.
[15] K. Seweryn, F. L. Basmadji, and T. Rybus, "Space robot performance during tangent capture of an uncontrolled target satellite," *The Journal of the Astronautical Sciences*, vol. 69, no. 4, p. 1017–1047, 2022.
[16] F. Aghili, "Optimal trajectories and robot control for detumbling a non-cooperative satellite," *Journal of Guidance, Control, and Dynamics*, vol. 43, no. 5, pp. 981–988, 2020.
[17] R. A. Gangapersaud, G. Liu, and A. H. J. de Ruiter, "Detumbling a non-cooperative space target with model uncertainties using a space manipulator," *Journal of Guidance, Control, and Dynamics*, vol. 42, no. 4, pp. 910–918, 2019.
[18] G. Ma *et al.*, "Hand-eye servo and impedance control for manipulator arm to capture target satellite safely," *Robotica*, vol. 33, no. 4, 2015.
[19] T. Oki, S. Abiko, H. Nakanishi, and K. Yoshida, "Time-optimal detumbling maneuver along an arbitrary arm motion during the capture of a target satellite," in *2011 IEEE/RSJ International Conference on Intelligent Robots and Systems*, 2011, pp. 625–630.
[20] K. Seweryn *et al.*, "Validation of the robot rendezvous and grasping manoeuvre using microgravity simulators," in *IEEE International Conference on Robotics and Automation (ICRA)*, 2018, pp. 873–880.
[21] R. Vijayan, M. De Stefano, and C. Ott, "A detumbling strategy for an orbital manipulator in the post-grasp phase," in *IEEE International Conference on Robotics and Automation*, May 2022.
[22] R. Vijayan, M. De Stefano, and C. Ott, "Control of an orbital manipulator with reaction wheels for on-orbit servicing," *IFAC-PapersOnLine*, vol. 55, no. 38, 2022, 13th IFAC Symposium on Robot Control.
[23] J. Hollerbach and K. Suh, "Redundancy resolution of manipulators through torque optimization," *IEEE Journal on Robotics and Automation*, vol. 3, no. 4, pp. 308–316, 1987.
[24] J. Artigas *et al.*, "The OOS-SIM: An on-ground simulation facility for on-orbit servicing robotic operations," in *Robotics and Automation (ICRA), IEEE International Conference on*, May 2015, pp. 2854–2860.
[25] K. Seweryn and M. Banaszkiewicz, "Optimization of the trajectory of a general free-flying manipulator during the rendezvous maneuver," in *AIAA Guidance, Navigation and Control Conference and Exhibit*, 2008.
[26] G. Misra and X. Bai, "Task-constrained trajectory planning of free-floating space-robotic systems using convex optimization," *Journal of Guidance, Control, and Dynamics*, vol. 40, no. 11, 2017.
[27] Y. Xie *et al.*, "Obstacle avoidance and path planning for multi-joint manipulator in a space robot," *IEEE Access*, vol. 8, 2020.
[28] R. Lampariello *et al.*, "Tracking control for the grasping of a tumbling satellite with a free-floating robot," *IEEE Robotics and Automation Letters*, vol. 3, no. 4, pp. 3638–3645, 2018.
[29] F. Aghili, "Optimal control of a space manipulator for detumbling of a target satellite," in *2009 IEEE International Conference on Robotics and Automation*, 2009, pp. 3019–3024.
[30] M. Shibli, F. Aghili, and C.-Y. Su, "Modeling of a free-flying space robot manipulator in contact with a target satellite," in *Proceedings of 2005 IEEE Conference on Control Applications, 2005.*, 2005, pp. 559–564.
[31] A. Dietrich, C. Ott, and A. Albu-Schäffer, "An overview of null space projections for redundant, torque-controlled robots," *The International Journal of Robotics Research*, vol. 34, no. 11, pp. 1385–1400, 2015.
[32] A. Dietrich and C. Ott, "Hierarchical impedance-based tracking control of kinematically redundant robots," *IEEE Transactions on Robotics*, vol. 36, no. 1, pp. 204–221, 2020.
[33] O. Khatib, "Inertial properties in robotic manipulation: An object-level framework," *The international journal of robotics research*, vol. 14, no. 1, pp. 19–36, 1995.
[34] R. Featherstone and O. Khatib, "Load independence of the dynamically consistent inverse of the jacobian matrix," *The International Journal of Robotics Research*, vol. 16, no. 2, pp. 168–170, 1997.
[35] C. Ott, A. Kugi, and Y. Nakamura, "Resolving the problem of non-integrability of nullspace velocities for compliance control of redundant manipulators by using semi-definite lyapunov functions," in *IEEE International Conference on Robotics and Automation*, 2008, pp. 1999–2004.
[36] F. Caccavale, C. Natale, B. Siciliano, and L. Villani, "Six-dof impedance control based on angle/axis representations," *IEEE Transactions on Robotics and Automation*, vol. 15, no. 2, pp. 289–300, 1999.
[37] Z. Wang *et al.*, "On stability properties of nonlinear time-varying systems by semi-definite time-varying lyapunov candidates," *IFAC Proceedings Volumes*, vol. 41, no. 2, p. 1123–1128, 2008.
[38] A. Albu-Schaffer, C. Ott, U. Frese, and G. Hirzinger, "Cartesian impedance control of redundant robots: recent results with the dlr-light-weight-arms," in *2003 IEEE International Conference on Robotics and Automation (Cat. No.03CH37422)*, vol. 3, 2003, pp. 3704–3709 vol.3.
[39] A. Beyer *et al.*, "Caesar: Space robotics technology for assembly, maintenance, and repair," in *Proceedings of the International Astronautical Congress, IAC*, 2018.
[40] M. A. Roa *et al.*, "Eross: In-orbit demonstration of european robotic orbital support services," in *2024 IEEE Aerospace Conference*, pp. 1–9.
[41] R. Smith *et al.*, "Open dynamics engine," 2005.
[42] H. Mishra *et al.*, "Reduced euler-lagrange equations of floating-base robots: Computations, properties and applications," *IEEE Transactions on Robotics*, vol. 39, no. 2, pp. 1439–1457, 2023.

Ria Vijayan received her master's degree in Space Technology from Lulea Technological University in 2018. She then worked as a research assistant at the University of Wuerzburg, in the field of spacecraft formation flying until 2020. She joined the German Aerospace Center (DLR) in 2021 as a research engineer. She has been awarded the Amelia Earhart Fellowship 2024 for women in aerospace engineering. Her doctoral research at DLR, in affiliation with TU Wien, covers robotics, on-orbit servicing, dynamic modeling, nonlinear control, and optimization.

Marco De Stefano received the bachelor's degree in aerospace engineering and the master's degree in astronautical engineering from the University of Rome La Sapienza, in 2008 and 2011, respectively, and the Ph.D. degree in industrial innovation engineering from the University of Modena and Reggio Emilia, in 2019. His Ph.D. thesis has been selected as one of the four finalists of the 2020 Georges Giralt Award for the Best Ph.D. Thesis of Robotics in Europe. Since 2012, he is a researcher with DLR, heading the Floating-base robot control group since 2023 with main focus on space robot dynamics, control theory, and hardware-in-the-loop simulation.

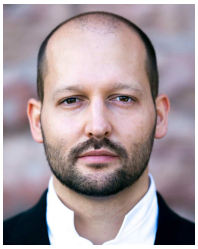

Alexander Dietrich received the doctoral degree from the Technical University of Munich, Germany, in 2015. He is currently head of the whole-body control group at the Institute of Robotics and Mechatronics of the German Aerospace Center. In 2016 he received the Georges Giralt Award for the best European PhD thesis in robotics. He is Editor of the IEEE ICRA, Associate Editor of the IEEE RAM and the IEEE RA-L, and he is co-chair of the IEEE RAS TC on Whole-Body Control. He currently holds a lecture at TUM on the control of modern lightweight robots. His research interests include robot control, humanoid robotics, mobile manipulation, and safe physical human-robot interaction.

Christian Ott received the Dr.-Ing. degree in control engineering from Saarland University, Saarbruecken, Germany, in 2005. From 2001 to 2007, he was with the German Aerospace Center (DLR), Institute of Robotics and Mechatronics. From May 2007 to June 2009, he worked as an Assistant Professor in the Department of Mechano-Informatics, University of Tokyo. From 2011 to 2016 he worked at DLR as a Team Leader of the group for Dynamic Control of Legged Humanoid Robots. From 2014 to 2022, he was Head of the Department of Analysis and Control of Advanced Robotic Systems at DLR. He is currently a Full Professor with TU Wien. His research interests include nonlinear robot control, flexible joint robots, impedance control, and control of humanoid robots.